J. Fluid Mech. (2004), *vol.* 503, *pp.* 47–56.
DOI: 10.1017/S0022112004008079 Printed in the United Kingdom

From laminar plumes to organized flows: the onset of large-scale circulation in turbulent thermal convection

By HENG-DONG XI, SIU LAM AND KE-QING XIA

Department of Physics, The Chinese University of Hong Kong, Shatin, Hong Kong, China

(Received 5 January 2004 and in revised form 14 January 2004)

We report an experimental study on the onset of the large-scale coherent mean flow in Rayleigh–Bénard turbulent convection. Shadowgraph and particle image velocimetry techniques are used to visualize the motion of thermal plumes and measure the velocity of the plumes and of the 'background' flow field, as the fluid motion evolves from quiescent to steady state. The experiment reveals the dynamical origin of the initial horizontal motion required by the large-scale flow: the fluid entrainment caused by the plume's vertical motion generates vortices surrounding the plume itself. These vortices in turn generate the initial horizontal motion of the flow field. Two types of interactions have been identified: (i) direct plume–vortex interaction; and (ii) plume–plume interaction via vortices. These interactions and the interaction and merging of the vortices from neighbouring plumes lead to groupings and/or merging of plumes, which in turn generate vortices of even larger scale. As a result of these interactions, the convective flow evolves into a coherent rotatory motion consisting of mainly the plumes themselves and spanning the whole convection box. This study clearly demonstrates that it is the thermal plumes that initiate the horizontal large-scale flow across the top and bottom conducting plates.

1. Introduction

A distinct feature of turbulent thermal convection in a closed box is a large-scale mean flow, or 'wind', that spans the height of the box and has a single cellular structure (at least in aspect-ratio-one boxes). Since its discovery by Krishnamurti & Howard (1981) through flow visualization, this so-called large-scale circulation (LSC) has been studied extensively. It is now generally believed that this LSC is driven or 'fed', interactively by the rising and falling thermal plumes that are generated at the convection cell's top and bottom plates. For example, Kadanoff (2001) likens the turbulent motion in the convection box to a machine and described the thermal plumes as both motors and heat pumps that drive the central bulk fluid and transport heat across the box. In fact, the idea that thermal plumes and the large-scale flow work together in a concerted fashion in the convective flow was recognized very early by several groups. Through semi-quantitative observation and estimations, Krishnamurti & Howard (1981) suggested that the LSC is driven by Reynolds stress associated with the tilting of plumes. In a later study, Zocchi, Moses & Libchaber (1990), using thermochromic liquid crystal microspheres, studied the 'life-cycle' of plumes and thermals, i.e. how they rise and fall in the cell in a synchronized fashion and interact with the flow field. More recently, Qiu & Tong (2001) have observed that the plumes, via their buoyancy, shear and drive the large-scale flow in a synchronized

way when they rise and fall along the opposite sidewalls, thus providing a self-feeding mechanism. Similar views have also been advanced by Niemela & Sreenivasan (2002), who suggested that the initial horizontal velocity comes from the pressure gradient associated with detachment of plumes. On the other hand, in systems with extremely low values of Prandtl number (Pr), such as mercury, the mean wind is also known to exist (Cioni, Ciliberto & Sommeria 1997) and it has been argued that plumes may not exist in these systems due to the large thermal conductivity of the fluid (Naert, Segawa & Sano 1997), which is plausible but so far has not been verified experimentally. The LSC in these systems may therefore be initiated and maintained by somewhat different mechanisms than the one described in this paper.

Note that large-scale flow in Rayleigh–Bénard convection exists not only in the very turbulent state but also near the onset of convective motion where the Rayleigh number Ra is just above the critical value for convection. For example, Charlson & Sani (1971) and Buell & Catton (1983) have made a linear stability analysis of a cylindrical fluid layer heated from below and found that the large-scale flow exists as a result of a preferred mode of the system. However, it is not clear that the large-scale flows in the near-onset and in the very turbulent regimes of convective flow are directly connected, and it is very likely they are not. For the large-scale circulatory flow in the turbulent state, there exists a large number of theoretical, experimental and numerical investigations on its various steady-state properties, for example, the velocity profile, the boundary layer thickness, its scalings with Ra, Pr and the geometry of the convection box, it spatial structures and their evolution with Ra, and the irregular reversal of its circulation directions (Castaing *et al.* 1989; Sano, Wu & Libchaber 1989; Tilgner, Belmonte & Libchaber 1993; Kerr 1996; Xin, Xia & Tong 1996; Takeshita *et al.* 1996; Cioni *et al.* 1997; Qiu & Xia 1998*a*, *b*; Verzicco & Camussi 1999; Ashkenazi & Steinberg 1999; Qiu, Yao & Tong 2000; Grossmann & Lohse 2000; Niemela *et al.* 2001; Sreenivasan, Bershadskii & Niemela 2002; Lam *et al.* 2002; Grossmann & Lohse 2002, 2003; Nimela & Sreenivasan 2003; Xia, Sun & Zhou 2003). For a more complete bibliography, see the recent review by Chavanne *et. al* (2001). For the transient behaviour of the flow before steady-state convection is attained, Neumann (1990) has made a numerical investigation on the time-dependent properties of Rayleigh–Bénard convection near the onset of convective flow over a wide range of Pr and for Ra below and above the critical value for convection. But there seems to be no investigation reported in the literature that studies the transient properties of the LSC in the turbulent regime before steady-state convection is reached.

In this paper, we focus on the origin of the large-scale flow and what made the plumes tilt and then participate and drive the mean flow. In other words, did the plumes initiate the flow or did an *a priori* flow sweep the plumes horizontally first? Intuition would tell us that, under the influence of a buoyant force, the plumes should move vertically rather than horizontally. To answer these questions, we study the transient behaviour of the large-scale mean flow through both particle image velocimetry (PIV) measurements of the velocity field and shadowgraph visualization of the thermal plumes. We present direct evidence to show that the mean wind is initiated by the thermal plumes. Specifically, we find that large-scale eddies are formed by the merging of vortices that are generated by the entrainment of fluid when plumes rise and fall vertically in the convection cell.

2. Experimental apparatus and methods

Two convection cells are used in the experiment: both are vertical cylinders and are identical except for their dimensions. The one used in the shadowgraph experiment has

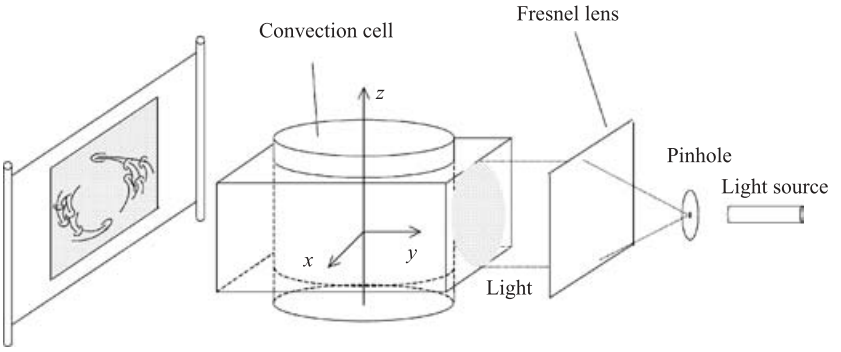

FIGURE 1. Schematic drawing of the experimental setup for shadowgraph visualizations.

a height of 15 cm and inner diameter 14 cm. The other, used in the PIV measurement, has a height 19.6 cm and diameter 19 cm (the aspect ratio for both is thus $\sim$1). The details of the convection cells are described by Lui & Xia (1998). Briefly their top and bottom plates are made of 2 cm thick copper with gold-plated surfaces and their sidewalls are made of a Pyrex glass tube. The working fluid used in the experiment is Dipropylene Glycol. This fluid is chosen mainly because its index of refraction has a relatively strong temperature dependence and thus is able to produce a large shadowgraphic contrast compared to fluids such as water. Figure 1 shows the setup for the shadowgraph visualization of thermal plumes, together with the coordinates used in the experiment. The light source is white light from a halogen lamp. The light first passes through a pinhole and then a Fresnel lens so that a uniform and collimated beam of light is shone through the cell. On the other side of the cell, the shadowgraph is observed on a wax-paper screen and is captured by a CCD camera. To prevent the distortion of the image due to the curvature of the cell wall, a rectangular shaped jacket made of flat glass plate is fitted to the outside of the cell wall. The jacket is filled with the same convecting fluid as in the cell. This greatly reduced the distortion effect. The Cartesian coordinate is so defined that its origin is at cell centre and the LSC coincides with the (x, z)-plane with z pointing up. Because the light is not focused onto a specific plane, the projected image on the screen is simply an integration of refractive index contrast along the lightpath (i.e. along the y-direction). To reduce the effect of light intensity inhomogeneity and other optical imperfections, the shadowgraph is divided pixel by pixel by a background image that is taken before the temperature gradient is imposed. The obtained image is then rescaled and smoothed. The PIV system has been described previously by Xia *et al.* (2003); in the present case the seeding particles are $8 \sim 12\,\mu$m diameter hollow glass spheres density matched to the convecting fluid (Lam *et al.* 2002) and the laser lightsheet (thickness $\sim$ 2 mm) is shone through the rotational plane of the LSC (the x,z plane). The two-dimensional velocity field is obtained by cross-correlating two consecutively measured images separated by a time interval of 55 ms at a sampling rate of 2 Hz.

To facilitate the study, we have tilted the convection cell by a small angle ($\leqslant 1^\circ$) so that the large-scale flow will be locked in a fixed plane (the x, z plane in this case). We find that both the titled and untilted cases show the same transient behaviour and the same final steady-state convective flow, the only difference is that in the tilted case LSC emerges in a shorter time period (50 min vs 100 min). To study the transient behaviour and the onset of the large-scale flow, recording of the shadowgraph images on the videotape recorder was started simultaneously with the switch-on of the heater and

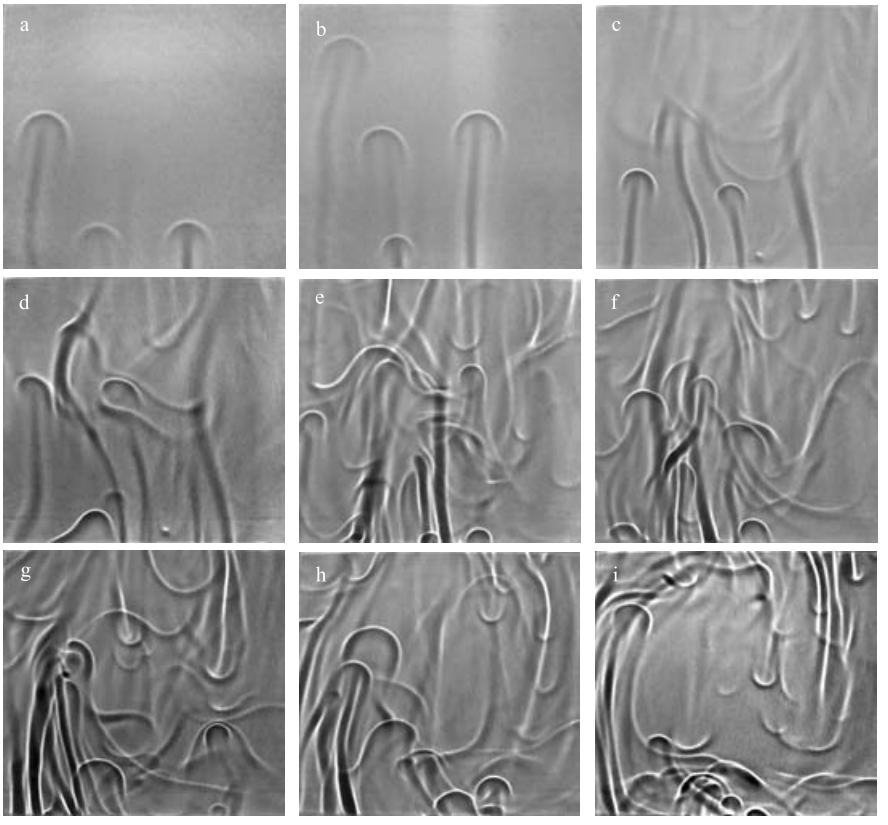

FIGURE 2. Shadowgraph images of plume motion at various stages of the transient process: (*a*) $t = 3$ min 58 s, (*b*) 4 min 25 s, (*c*) 11 min 26 s, (*d*) 11 min 41 s, (*e*) 27 min 13 s, (*f*) 27 min 40 s, (*g*) 29 min 24 s, (*h*) 30 min 05 s, and (*i*) 44 min 52 s.

cooler that are attached, respectively, to the bottom and top plates of the convection box with the fluid inside in a quiescent state. This moment is denoted as time $t = 0$. The recording lasted for more than two hours at which time the flow pattern is firmly established, thus enabling us to capture the entire transient process from the generation of the first plumes to the organized steady flow of the thermal plumes. As in the shadowgraph case, the PIV measurement started simultaneously with the switch-on of the cooler and heater and lasted for ~130 min. When the fluid reaches steady-state convection, the Rayleigh and Prandtl numbers for the shadowgraph experiment are $Ra = 6.8 \times 10^8$ and $Pr = 596$, respectively; and for the PIV experiment they are $Ra = 8.3 \times 10^8$ and $Pr = 1032$, respectively. Although the shadowgraph and the PIV measurements reached different steady-state convection, both started from the same initial conditions and we believe the difference in the Ra and Pr values does not affect our conclusions about the mechanism for the onset of LSC.

3. Results and discussion

3.1. *Shadowgraph studies*

Figure 2 shows shadowgraph images taken during the various stages of the transient process. In panels (*a*) and (*b*) we see the first appearance of "laminar' plumes that move straight up without any visible wavy-like motion. This can be classified as the

first stage of the transient process. Panels (*c*) and (*d*) show examples of the second stage where the plumes start to have wavy-like motions, but are still mostly upward going and there is definitely no horizontal sweeping. Panels (*e*) and (*f*) show the third stage of the transient process in which the ascending hot plumes and descending cold plumes still move mostly vertically and appear to be distributed randomly in space, but there are clearly more interactions among the plumes. Panels (*g*), (*h*) and (*i*) show the fourth stage of the transient process, in which the plumes start to organize spatially: the hot ones rising along the left sidewall and the cold ones falling along the right sidewall. As a result, the flow gradually evolved a clockwise rotary motion. Note that due to the finite heat capacity of the water-bath circulator and the fact that the cooling capacity of refrigerated circulators decreases as the temperature decreases, the top plate reaches its steady-state temperature much slower than the bottom plate, which means a thermal boundary layer will build up near the bottom plate before it is formed near the top plate. This is manifested by the fact that only hot plumes are generated initially in the shadowgraph and PIV studies (see below). Because of this asymmetry in the development of the top and bottom boundary layers, the details of the several transient stages and the time at which they occur may be different if both hot and cold plumes are generated at the same time shortly after the start of the experiment. For example, the time origin might be shifted to the moment at which both hot and cold plumes are generated in the same quantity. However, the main conclusion of the paper that the mean wind (or the LSC) is initiated and maintained by the thermal plumes should remain unchanged.

3.2. *Particle image velocimetry measurements*

Because the shadowgraphs are based on refractive index contrast, they do not show directly the motion of the background fluid but only those of the 'thermal objects' like plumes. To eliminate the possibility that the plumes' horizontal motions are initiated by a possible background horizontal velocity existing prior to their motion and invisible in the shadowgraphs, we make a direct measurement of the velocity field in the (x, z)-plane in which the large-scale circulation would appear when steady-state motion is attained. Figure 3 shows the 'instant' two-dimensional velocity field measured in the early stage of the transient process, where the velocity magnitude is coded by colour and by the length of the vector in $\mathrm{cm\,s^{-1}}$. Since the flow speed is very low, to obtain a good 'signal-to-noise ratio' each velocity field in the figure is an average of 5 consecutive measurements over a period of 2.5 s. Because of the low velocity the plumes have not moved significantly over this time period; we can thus take this short-time-averaged result as an instantaneous measurement and all the 'instant' velocity maps presented below are averaged this way. Figure 3 shows the motions of four thermal plumes as they traverse the height of the convection cell. A few features may be noted: (i) Before the rise of plumes the fluid is essentially quiescent; in fact all velocity maps measured prior to the appearance of plumes look the same as the top half of panel (*a*), which is indistinguishable from the result for a fluid at rest with no imposed temperature gradient. (ii) The plumes' motions are confined in a vertical plane at this stage; since the thickness of the laser lightsheet is only about 2 mm, if the plumes had significant velocity in the y-direction they would have moved out of the lightsheet by the time they had travelled over half the height of the cell. (iii) By pushing and entraining the fluid as they move, the plumes generate vortices around themselves and thus create the initial horizontal motion of the fluid. (iv) The plumes in turn interact with the vortices surrounding them, which makes the plumes' initial pure vertical motions unstable and produces horizontal movement.

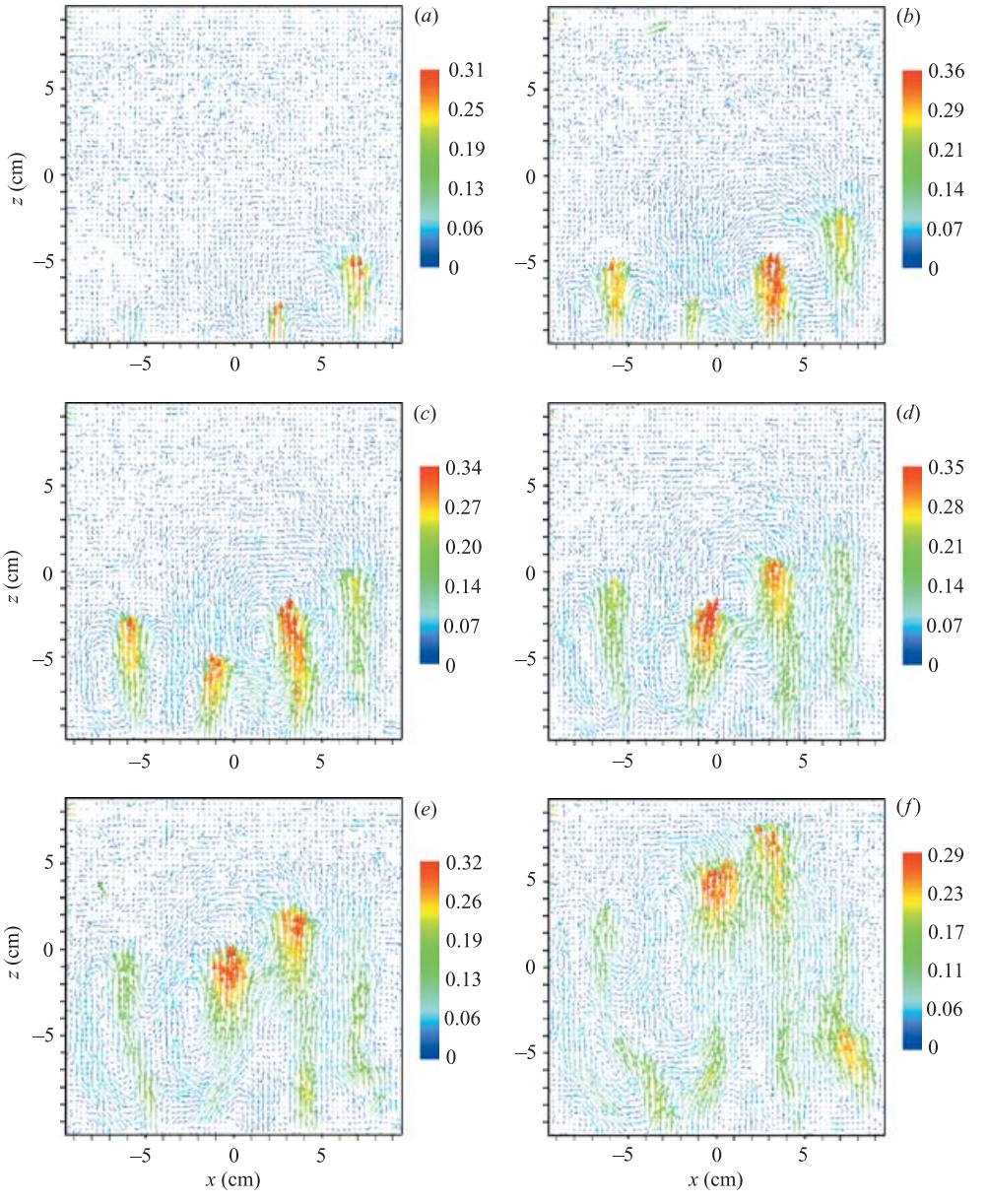

FIGURE 3. Instant velocity fields, in unit of cm s^{-1}, showing the emergence of the first few plumes at time (*a*) $t = 5$ min, (*b*) 5 min 12 s, (*c*) 5 min 25 s, (*d*) 5 min 37 s, (*e*) 5 min 50 s and (*f*) 6 min 15 s.

There appear to be two types of interactions here. In the first one, plumes interact directly with the vortices generated by them. As an example, we track the motion of the leftmost plume in figure 3(*b*) which has an initial horizontal position of $x \approx -5.5$ cm. As this plume moves upward, the down-rightward flow generated by the vortex to its left pushes its stem to the right as shown by panels (*c–f*). As a result, its stem ends up at $x \approx -3.5$ cm in panel (*f*) (note that the horizontal position of the cap of this plume did not change much during this period, it is now at $x \approx -6.5$ cm and $z \approx 3.5$ cm). In

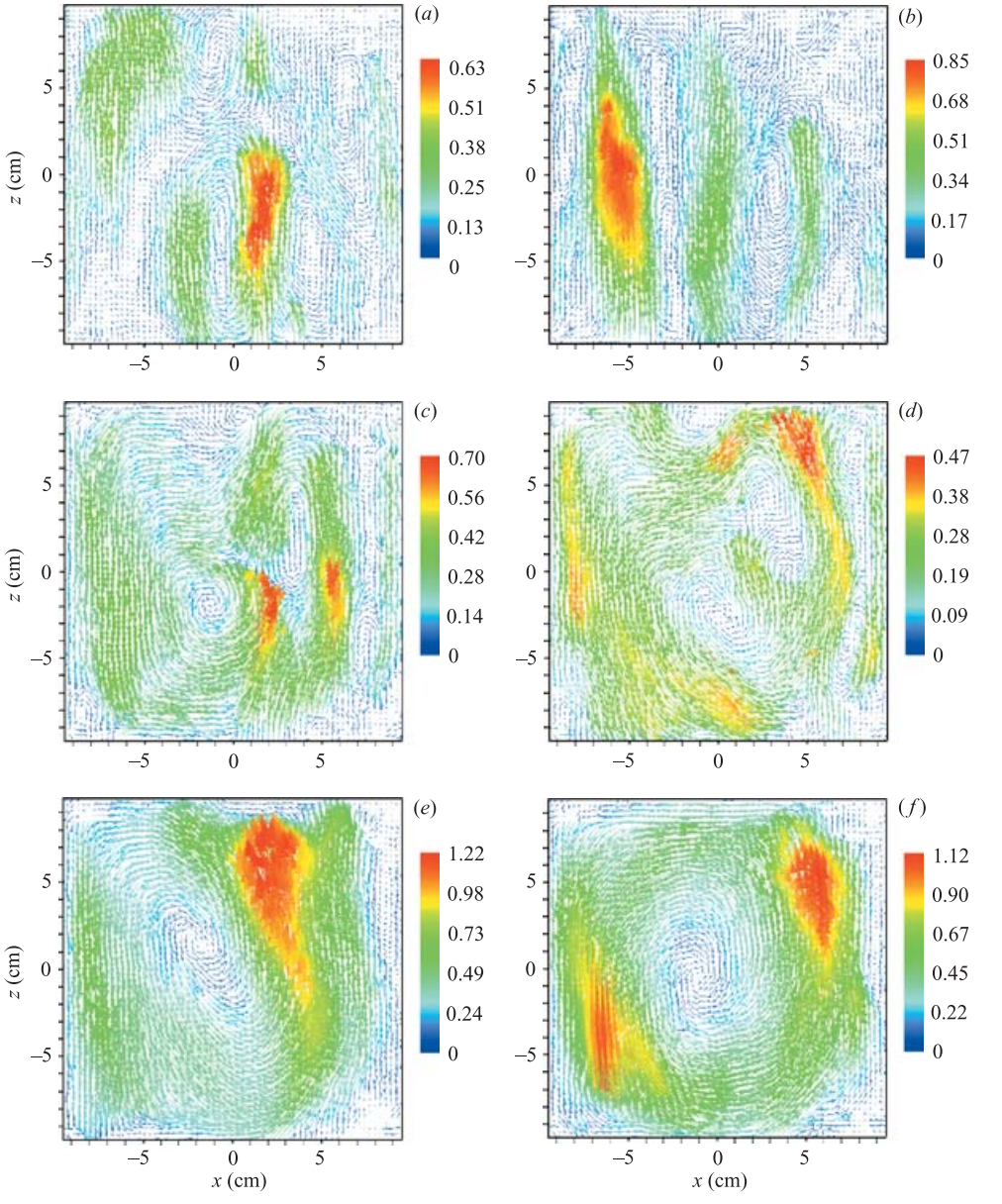

FIGURE 4. PIV-measured velocity fields at (*a*) $t = 27$ min 55 s, (*b*) 37 min 30 s, (*c*) 45 min 45 s, (*d*) 46 m 25 s, (*e*) 47 m 45 s and (*f*) 117 min 5 s.

the second type plumes interact with each other via the vortices they generate, which may also be viewed as interactions between vortices. The motion of the second plume from left in figure 3(*b*) provides an example of this type: it has an initial horizontal position of $x \approx -1.5$ cm and interacts with its two neighbouring plumes via their respective vortices and the result is a net force that pushes it to the right, as seen from panels (*c–e*). Finally, in panel (*f*) its cap ends up at $x \approx 0$ and $z \approx 6$ cm.

The interactions between plumes and the flow field and among the plumes themselves like the ones described above lead to the groupings and/or mergers of

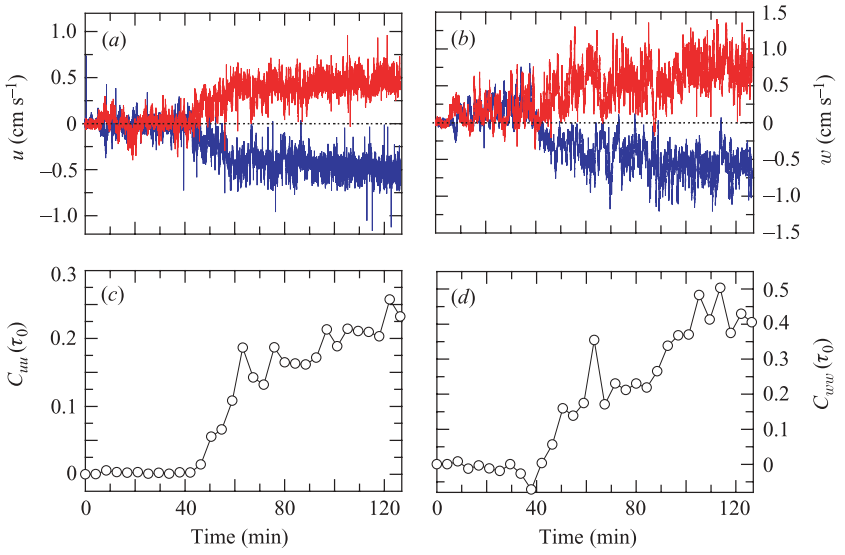

FIGURE 5. (*a*) Horizontal velocity at two points near the top (u_{top}, blue) and bottom (u_{bot}, red) plate respectively. (*b*) Vertical velocity near the left (w_{left}, blue) and right (w_{right}, red) sidewalls. (*c*) Time-dependent cross-correlation coefficient between u_{top} and u_{bot} and (*d*) that between w_{left} and w_{right}.

plumes which result in larger vortices and thus larger-scale fluid motions. Examples of these are shown in figure 4(*a*, *b*), which corresponds to the third stage of the transient process. The plumes now move in larger groups and produce larger vortices surrounding them, but their motion is still mostly vertical. As the plumes further interact with the flow field and among themselves via the vortices, their motion gradually evolves into a self-organized rotatory motion, examples of which are shown in figure 4(*c*–*f*). A single-roll counterclockwise rotatory motion emerges at $t \approx 40 - 50$ min, but the flow is still unstable at this stage and it takes about 2 hours before the flow becomes steady. Figure (*f*) shows an example of the velocity field at the steady state. The dynamics of the plume motions described here can be seen more clearly from the 'PIV movies' made by concatenating the consecutively measured 'instant' velocity fields.† (Note that the flow direction in the PIV is opposite to that shown in the shadowgraphs.)

The transient process described above can also be studied in a more quantitative way by examining the PIV-measured velocity time series at various points in the convection cell and the corresponding cross-correlation functions between them. Figure 5(*a*) plots the horizontal velocity $u(t)$ for the duration of the experiment at two points, one 2.6 cm below the centre of the top plate (u_{top}, blue trace) and the other 2.6 cm above the bottom plate (u_{bot}, red trace). Figure 5(*b*) plots the vertical velocity $w(t)$ at two points 2.6 cm from the opposite sidewall at midheight: w_{left} (blue trace) for the left sidewall and w_{right} (red trace) for the right sidewall. Here upward and rightward motions are defined as positive. These time series clearly show that after $40 \sim 50$ min velocities at these four points simultaneously become significantly non-zero and with directions that signify the emergence of a counterclockwise rotatory motion. This feature can also be seen by studying the short-time correlation function

† These movies can be viewed at http://www.phy.cuhk.edu.hk/turbulence

$C_{uu}(\tau) = \langle -u_{top}(t+\tau)u_{bot}(t)\rangle_{t_0}$ between the horizontal velocity near the top and bottom plates, where the average $\langle \ldots \rangle_{t_0}$ is over a time interval $t_0 = 250\,\mathrm{s}$ which corresponds to about four circulation times of the LSC. Similarly, we calculate $C_{ww}(\tau) = \langle -w_{left}(t+\tau)w_{right}(t)\rangle_{t_0}$. This definition will lead to positive correlations if there is counterclockwise motion. The peak of the cross-correlation function, $C(\tau_0)$ at certain value τ_0, is a measure of the degree of correlation between motion at the respective points, which is just the correlation coefficients. Figures 5(*c*) and 5(*d*) show respectively $C_{uu}(\tau_0)$ and $C_{ww}(\tau_0)$ for the same time period. Again, both show clearly that coherent motion starts at $t \approx 40 \sim 50\,\mathrm{min}$, in agreement with visual observations from shadowgraphs and PIV vector maps. The figures also reveal that it takes about 2 hours for the flow to stabilize.

4. Conclusions

We experimentally studied the onset of the large-scale coherent flow in Rayleigh–Bénard turbulent convection, using a high Prandtl number liquid as the convecting fluid. Shadowgraph and PIV techniques are used to visualize the motion of thermal plumes and measure the velocity of the plumes and the 'background' flow field, respectively. The study reveals the dynamical origin of the initial horizontal motion required by the large-scale flow and shows how the fluid motion evolves from a quiescent state to a steady state as a temperature difference is imposed across the convection cell. The shadowgraph study clearly shows that the LSC is a result of the organization of the plume motion, i.e. the interaction between the plumes leads to the spatial separation of hot and cold plumes, which in turn leads to the rotatory motion of the large-scale flow. The PIV measurements further reveal that it is the fluid entrainment due to the plume's vertical motion that generates vortices which in turn generate the initial horizontal motion of the fluid. The interaction and merging of the vortices from neighbouring plumes lead to groupings and/or merging of the plumes themselves, which in turn generate vortices of even larger scale. We have identified two types of plume interactions: (i) plumes interact directly with the vortices generated by themselves and (ii) plumes interact with each other via the vortices they generate (which is also a type of vortex–vortex interaction). As a result of the plume–vortex and plume–plume interactions, the fluid finally evolves a coherent rotatory motion consisting mainly of plumes themselves and spanning the whole convection box. This study clearly demonstrates that it is the thermal plumes that initiate the horizontal large-scale flow across the top and bottom conducting plates and that the mean wind is simply the organized motion of plumes.

We are pleased to acknowledge support of this work by the Hong Kong Research Grants Council under Project No. CUHK4242/01P.

REFERENCES

Ashkenazi, S. & Steinberg, V. 1999 High Rayleigh number turbulent convection in a gas near the gas-liquid critical point. *Phys. Rev. Lett.* **83**, 3641–3644.

Buell, J. C. & Catton, I. 1983 The effect of wall conduction on the stability of a fluid in a right circular cylinder heated from below. *J. Heat Transfer* **105**, 255–260.

Castaing, B., Gunaratne, G., Heslot, F., Kadanoff, L., Libchaber, A., Thomae, S., Wu, X. Z., Zaleske, A. & Zanetti, G. 1989 Scaling of hard thermal turbulence in Rayleigh–Bénard convection. *J. Fluid Mech.* **204**, 1–30.

Charlson, G. S. & Sani, R. L. 1971 On thermoconvective instability in a bounded cylindrical fluid layer. *Intl J. Heat Mass Transfer*. **14**, 2157–2160.

Chavanne, X., Chillà, F., Chabaud, B., Castaing, B. & Hébral, B. 2001 Turbulent Rayleigh–Bénard convection in gaseous and liquid He. *Phys. Fluids* **13**, 1300–1320.

Cioni, S., Ciliberto, S. & Sommeria, J. 1997 Strongly turbulent Rayleigh–Bénard convection in mercury: comparison with results at moderate Prandtl number. *J. Fluid Mech.* **335**, 111–140.

Grossmann, S. & Lohse, D. 2000 Scaling in thermal convection: a unifying view. *J. Fluid Mech.* **407**, 27–56.

Grossmann, S. & Lohse, D. 2002 Prandtl and Rayleigh number dependence of the Reynolds number in turbulent thermal convection. *Phys. Rev.* E **66**, 016305.

Grossmann, S. & Lohse, D. 2003 On geometry effects in Rayleigh-Bénard convection. *J. Fluid Mech.* **486**, 105–114.

Heslot, F., Castaing, B. & Libchaber, A. 1987 Transitions to turbulence in helium gas. *Phys. Rev.* A **36**, 5870–5873.

Kadanoff, L. P. 2001 Turbulent heat flow: Structures and scaling. *Physics Today* **54**(8), 34–39.

Kerr, R. M. 1996 Rayleigh number scaling in numerical convection. *J. Fluid Mech.* **310**, 139–179.

Krishnamurti, R. & Howard L. N. 1981 Large-scale flow generation in turbulence convection. *Proc. Natl Acad. Sci. USA* **78**, 1981–1985.

Lam, S., Shang, X.-D., Zhou, S.-Q. & Xia, K.-Q. 2002 Prandtl number dependence of the viscous boundary layer and the Reynolds numbers in Rayleigh-Bénard convection. *Phys. Rev.* E **65**, 066306.

Lui, S.-L. & Xia, K.-Q. 1998 Spatial structure of the thermal boundary layer in turbulent convection. *Phys. Rev.* E **57**, 5494–5503.

Naert, A., Segawa, T. & Sano, M. 1997 High-Reynolds-number thermal turbulence in mercury. *Phys. Rev.* E **56**, R1302–R1305.

Neumann, G. 1990 Three-dimensional numerical simulation of buoyancy-driven convection in vertical cylinders heated from below. *J. Fluid Mech.* **214**, 559–578.

Niemela, J. J., Skrbek, L., Sreenivasan, K. R. & Donnelly, R. J. 2001 The wind in confined thermal convection. *J. Fluid Mech.* **449**, 169–178.

Niemela, J. J. & Sreenivasan, K. R. 2002 Thermal fluctuations and their ordering in turbulent convection. *Physica* A **315**, 203–214.

Niemela, J. J. & Sreenivasan, K. R. 2003 Rayleigh-number evolution of large-scale coherent motion in turbulent convection. *Europhys. Lett.* **62**, 829–833.

Qiu, X.-L. & Tong, P. 2001 Large-scale velocity structures in turbulent thermal convection. *Phys. Rev.* E **64**, 036304.

Qiu, X.-L. & Xia, K.-Q. 1998*a* Viscous boundary layers at the sidewall of a convection cell. *Phys. Rev.* E **58**, 486–491.

Qiu, X.-L. & Xia, K.-Q. 1998*b* Spatial structure of the viscous boundary layer in turbulent convection. *Phys. Rev.* E **58**, 5816–5820.

Qiu, X.-L., Yao, S.-H. & Tong, P. 2000 Large-scale coherent rotation and oscillation in turbulent thermal convection. *Phys. Rev.* E **61**, R6075–R6078.

Sano, M., Wu, X.-Z. & Libchaber, A. 1989 Turbulence in helium-gas free convection. *Phys. Rev.* A **40**, 6421–6430.

Sreenivasan, K. R., Bershadskii, A. & Niemela, J. J. 2002 Mean wind and its reversal in thermal convection. *Phys. Rev.* E **65**, 056306.

Takeshita, T., Segawa, T., Glazier, J. A. & Sano, M. 1996 Thermal turbulence in mercury. *Phys. Rev. Lett.* **76**, 1465–1468.

Tilgner, A., Belmonte, A. & Libchaber, A. 1993 Temperature and velocity profiles of turbulent convection in water. *Phys. Rev.* E **47**, R2253–R2256.

Verzicco, R. & Camussi, R. 1999 Prandtl number effects in convective turbulence. *J. Fluid Mech.* **383**, 55–73.

Xia, K.-Q., Sun, C. & Zhou, S.-Q. 2003 Particle image velocimetry measurement of the velocity field in turbulent thermal convection. *Phys. Rev.* E **68**, 066303.

Xin, Y.-B., Xia, K.-Q. & Tong, P. 1996 Measured velocity boundary layers in turbulent convection. *Phys. Rev. Lett.* **77**, 1266–1269.

Zocchi, G., Moses, E. & Libchaber, A. 1990 Coherent structures in turbulent convection, an experimental study. *Physica* A **166**, 387–407.